# Investigation of Wall-Pressure Fluctuations Characteristics on a NACA0012 Airfoil with Blunt Trailing Edge

A. Grébert* and J. Bodart† and L. Joly ‡

*Université de Toulouse, ISAE-Supaero, BP 54032, 31055 Toulouse Cedex 04, France*

**The trailing edge noise, or the so-called self-noise of an airfoil, significantly contributes to the broadband noise in various configurations such as high bypass-ratio engines and counter-rotating open rotors. The present work aims at characterizing the wall-pressure fluctuations in the turbulent boundary layer just upstream the trailing edge, that are known to shape the trailing edge noise spectrum. These investigations are carried out using large-eddy simulations, with the massively parallel compressible solver CharLES$^X$, of the flow over a truncated NACA0012 airfoil at $Re_c = 4 \times 10^5$ for angles of attack $\alpha = 0°$ and $\alpha = 6.25°$. Unsteady wall-pressure signals are recorded using several thousands of probes distributed over the suction side. We focus on data-processing the pressure signals to extract quantities crucial to trailing edge noise modelling: the convection velocity $U_c$, the spanwise correlation length $l_z$ and the spectrum of the wall-pressure fluctuations $\Phi_{pp}$.**

## I. Introduction

BROOKS et al.[1] identified the turbulent boundary layer-trailing edge interaction, as one of the five self-noise mechanisms, which finds its origin in the scattering of the vortical structures in the turbulent boundary layer (TBL) by the trailing edge bluntness. The theoretical treatment of this noise mechanism generally relies on Amiet[2,3] and Howe[4] theories. Accurately predicting the trailing edge noise still faces significant issues: most of the modelling involves empirical and semi-empirical models[5–8] which are essentially relying on the pressure footprint at the wall of the upstream TBL. These methods were used by Brooks and Hodgson[5] who found a good agreement of their sound pressure measurements in the farfield with the predictions of Howe[4], derived from the wall-pressure field. The results obtained with the model of Howe[4] or Amiet[2], later enhanced by Roger and Moreau[9], have been successfully compared to farfield sound pressure measurements by Moreau and Roger[10]. These models rely on a small set of quantities describing the fluctuating pressure in the TBL, namely the spectrum $\Phi_{pp}$, the convection velocity $U_c$ and the spanwise correlation length scale $l_z$ of the surface pressure fluctuations. These quantities are difficult to measure experimentally and an accurate assessment of these model parameters using large-eddy simulations is an option towards more reliable and robust predictions. This is the objective of the present study which aims at characterizing these quantities in the particular case of a NACA0012 airfoil.

In the last decades, numbers of experiments and empirical models have been developed to characterize the convection velocity $U_c$ of turbulent structures responsible for the wall-pressure fluctuations. This so-called convective velocity is usually derived from the space-time correlation function yielding expressions of $U_c(\omega, \varepsilon_1)$ depending on both the temporal frequency, which may be related to the structure size through Taylor's hypothesis, and a streamwise separation distance $\varepsilon_1$. According to Amiet[2], $U_c$ can be reasonably expressed as a weak function of the temporal frequency of the local pressure signal and assumed to be correctly represented by a constant value $U_c \approx 0.8U_e$, $U_e$ being the velocity at the edge of the boundary layer.

*PhD student, DAEP, ISAE-Supaero, 31055 Toulouse Cedex 04, France - arnaud.grebert@isae.fr
†Ass. Professor, DAEP, ISAE-Supaero, 31055 Toulouse Cedex 04, France
‡Professor, DAEP, ISAE-Supaero, 31055 Toulouse Cedex 04, France

However, Brooks and Hodgson[5] performed a comprehensive experimental investigation of trailing edge noise in the case of a two-dimensional airfoil and reported that the convection velocity is both sensitive to the longitudinal separation distance and the frequency. Farabee and Casarella[11] experimental measurements of the frequency spectra and cross-spectra of the wall-pressure fluctuations beneath a turbulent boundary layer gave further insights about the physical meaning of the convection velocity. They obtained $U_c$ from the phase $\varphi$ of the wall-pressure cross-spectrum using the relation $\varphi(\varepsilon_1, \omega) = -\omega\varepsilon_1/U_c$. The convection velocity was thus demonstrated to depend on the separation distance and frequency. They pointed out that the classical Taylor's hypothesis of "frozen turbulence" hardly holds in boundary layers where all eddies are not advected at a unique velocity. Instead, they identified a clear dependency of $U_c$ on the temporal frequency for the lower range of frequency and on the separation distance for small distances. Leclercq and Bohineust[12] performed experiments in an anechoic wind-tunnel facility to characterize the wall-pressure fluctuations on a flat plate with a refined spatio-temporal resolution. They were able to discuss the relationship between the frequency of the wall-pressure fluctuations, associated with coherent structures, with the length scale or the convection velocity of theses structures. In turbulent boundary layers where the mean velocity significantly varies across the flow, long living large eddies and short life-time small ones do not necessarily travel at same velocities. They also do not have the same radius of impact on the pressure field. Small eddies, associated with high frequencies and small streamwise correlation distances, have to fly closer to the wall, at consequently low convection velocities, to impart significant wall-pressure fluctuations. Large eddies of the size of the boundary layer thickness yield wall-pressure fluctuations at lower frequencies from places more remote from the wall thus associated with larger convective velocities of the order of $U_\infty$. They also feed the pressure cross-spectra at larger streamwise separation distances. Following these considerations, it is expected that $U_c$ increases with the streamwise separation distance $\varepsilon_1$ and decreases with the frequency. Eventually, the scale separation between large and small structures in the inner layer of the TBL necessarily requires to sensitize refined models for $U_c$ to the Reynolds number.

The approach developed by Amiet[2] and Howe[4] is based on the surface pressure field which bridges the gap between local hydrodynamic quantities at some distance upstream of the trailing-edge to the features of the farfield acoustic pressure spectrum. In this perspective, the surface pressure fluctuation normalized spectrum $\Phi_{pp}(\omega)$ is another key ingredient required to build up trailing edge noise models. In these models, the wall-pressure fluctuations are used as wall footprints of moving acoustic sources and several models[13,14] have been developed to predict the resulting $\Phi_{pp}(\omega)$. Experiments such as the one by Leclercq and Bohineust[12] aimed at providing reference measurements to help calibrate these models. The last quantity of interest to complete these TE noise models is the spanwise correlation length $l_z$ of the wall-pressure fluctuations. Simple models[15] for this length scale use dimensional analysis using the frequency and the convection velocity to write $l_z = U_c/\omega\alpha$, in which $\alpha$ is an adjustable non-dimensionnal parameter. This expression agrees fairly well with experimental data at high frequencies but no consensus on $\alpha$ has been adopted by the community as $\alpha$ varies significantly with the experimental or numerical framework and the model adopted for the convection velocity. In particular, using a constant value for $U_c$ leads to a nonphysical behavior of the model for $l_z$ at low frequencies. Combined choices for the values of $U_c$ and $\alpha$ from the literature have been summarized in Table 1 which highlights the scattering of the model parameters. Interestingly, Howe[4] reported that for low to moderate Mach number, the farfield noise in the mid-span plane may be predicted from the wall-pressure spectrum $\Phi_{pp}(\omega)$ upstream of the trailing edge and the spanwise correlation length $l_z(\omega)$, as used by Nodé-Langlois[7] for trailing edge broadband noise.

The present work aims at providing a new set of data, highly resolved in space and time, to help developing more accurate TE noise prediction models. We propose to characterize the pressure fluctuations in a TBL over a truncated NACA0012 airfoil and to focus on the three model ingredients previously mentioned. The numerical set-up and the flow solver are described in the following section with an emphasis on the tripping method used to trigger laminar-turbulent transition. Validation of the grid resolutions is carefully reported as well as the pressure data acquisition method and the influence of span extent of the numerical domain. These best trade-offs are then adopted to perform final simulations for two angles of attack.

**Table 1. Convection velocity and Corcos[15] model constant used for different airfoil experiments. In bold the case considered from Sagrado[16]'s work and in red the extreme values of Corcos[15] model constant and convection velocity $U_c$.**

| Airfoil (Reference) | $\alpha = 1/b$ | $U_c/U_\infty$ | $Mach$ | $Re_c$ |
|---|---|---|---|---|
| NACA0012 Airfoil (Brooks and Hodgson[5]) $\alpha = 0°$ | 0.625 | 0.60 | 0.11 | $1.56 \times 10^6$ |
| NACA0012 Airfoil (Brooks and Hodgson[5]) $\alpha = 0°$ | 0.581 | 0.60 | 0.20 | $2.80 \times 10^6$ |
| **NACA0012 Airfoil (Sagrado[16]) $\alpha = 0° - 6.25°$** | **0.665** | **0.69** | **0.05** | $\mathbf{4.00 \times 10^5}$ |
| NACA64-618 Airfoil (Fischer[17]) $\alpha = 2.6° - 3.1°$ | 0.714 | 0.70 | 0.09-0.18 | $1.71 - 2.85 \times 10^6$ |
| Valeo CD Airfoil (Roger and Moreau[18]) $\alpha = 13°$ | 0.665 | 0.60 | 0.05 | $1.44 \times 10^5$ |
| Valeo CD Airfoil (Moreau and Roger[19]) $\alpha = 15°$ | 0.833 | 0.75 | 0.05 | $1.38 \times 10^5$ |
| Valeo CD Airfoil (Moreau and Roger[19]) $\alpha = 8°$ | 0.665 | 0.70 | 0.05 | $1.38 \times 10^5$ |
| V2 Airfoil (Rozenberg et al.[20]) $\alpha = 0°$ | 0.714 | 0.65 | 0.05 | $1.44 \times 10^5$ |
| Fan Blade mid span (Rozenberg[21]) | 0.714 | 0.75 | 0.05 | $1.38 \times 10^5$ |

# II. Flow solver

The present large-eddy simulations (LES) were performed using the massively parallel CharLES$^X$ solver which solve the spatially filtered compressible Navier-Stokes equations for the conserved variables of mass, momentum and total energy using a finite volume formulation, control-volume based discretisation in unstructured hexahedral meshes. An explicit third-order Runge-Kutta (RK3) is used for time advancement (see Bermejo-Moreno et al.[22] for more details in the numerics). The solver has been used to study reactive[23] and high Reynolds number flows[24]. It includes Vreman[25] subgrid-scale (SGS) model to represent the effect of unresolved small-scale fluid motions.

In order to be consistent with Sagrado[16]'s experiments (see Table 2), a laminar to turbulent transition is imposed at a fixed $x_{tr}$ location. No modification is added to the geometry or the mesh, but a sponge-like source term is added to the Navier-Stokes equations: we locally force the solution towards a flow at rest in the transition region:

$$\begin{aligned}
&\frac{\partial \rho}{\partial t} + \frac{\partial}{\partial x_j}(\rho u_j) = \sigma(\rho_{ref} - \rho) \\
&\frac{\partial \rho u_i}{\partial t} + \frac{\partial}{\partial x_j}(\rho u_i u_j + p\delta_{ij} - \tau_{ij}) = \sigma\left[(\rho u_i)_{ref} - \rho u_i\right] \\
&\frac{\partial E}{\partial t} + \frac{\partial}{\partial x_j}\left[(E+p)u_j + q_j - u_k\tau_{kj}\right] = \sigma(E_{ref} - E)
\end{aligned} \tag{1}$$

where $\rho$, $u_i$, $p$, $E$, $\tau_{ij}$ and $q_j$ are the density, velocity, pressure, total energy, viscous stress tensor and heat flux, respectively. The source terms on the right-hand side are made active only near the external boundaries. $1/\sigma$ is the characteristic time scale of the forcing and set to the same value for all conserved variables. To match stability constraints we set $\sigma \approx 1/\Delta t$, where $\Delta t$ is the timestep of the computation. The active region in the present work covers the entire span and is a square box with dimensions $0.25\delta \times 1\delta$ in streamwise and wall-normal directions. The large value of the source term extent in the wall normal direction ($1\delta$) is chosen consistently with Sagrado[16]'s experiments at low Reynolds number of $Re_c = 4 \times 10^5$ considered for the present LES.

# III. Numerical set-up

## III.A. Investigated configuration

The present work is based on Sagrado[16]'s experiments, performed at the Whittle Laboratory of the University of Cambridge. This test case has been chosen mainly because of the large database available and the extensive analysis performed on the parameters of primary interest to this work. Furthermore, the NACA0012 airfoil geometry has been extensively studied and documented in the literature, which allows in-depth validation of the results and numerical strategies.

Sagrado[16] used a truncated NACA0012 profile to create a blunt trailing edge. Various trailing edge thicknesses were investigated but we currently focus on the case with a bluntness parameter $h/\delta^*$ above 0.3, so-called blunt TE, to enable a vortex shedding at the trailing edge, identified as an additional noise source by Brooks and Hodgson.[5]

Table 2 summarizes the flow conditions considered for the present work and identical to Sagrado[16]'s experiments. We consider two angles of attack $\alpha = [0°, 6.25°]$ for which no flow separation occurs. The tripping of the boundary layer is kept consistent with the experiments, and a transition from laminar to turbulent is imposed at a location of $x_{tr} = 0.127c$, using the above described method. Note that in this case, natural transition has been reported[16] to occur much further downstream at $x_{tr} \approx 0.75c$, which would not be suitable for the study of noise models for fully developed turbulent boundary layers.

**Table 2. Geometrical parameters based on Sagrado[16]'s experiments and numerical parameters of the present work.**

| Geometry | $Re_c$ | $M_\infty$ | TE thickness $h/c$ | $x_{tr}/c$ | $\alpha$ |
|---|---|---|---|---|---|
| NACA0012 | $4 \times 10^5$ | 0.05 | $5.4 \times 10^{-3}$ | 0.127 | $[0°, 6.25°]$ |

## III.B. Grid design

**Table 3. Typical mesh sizes (expressed in wall units) requirements for a boundary layer flow using DNS and wall-resolved LES (Wagner et al.[26]) and current LES grid resolution.**

| Direction | Grid spacing | DNS | Wall-resolved LES | Current LES |
|---|---|---|---|---|
| Streamwise | $\Delta x^+$ | 10-15 | 50-150 | 30 |
| Spanwise | $\Delta z^+$ | 5 | 10-40 | 10-20 |
| Wall-normal | $\min(\Delta y^+)$ | 1 | 1 | 1 |
| Number of points in | $0 < y^+ < 10$ | 3-5 | 3-5 | 5 |

The unstructured grid has a CH-type topology as shown in Figure 1. The mesh includes both structured and unstructured blocks. Block 1 to 4 are structured blocks whereas block 5 to 7 are unstructured and composed of quads. The C part of the domain extend up to 20 chords upstream, above and below the airfoil, the length of the H part is also 20 chords downstream. The structured block 2 is designed to contain the entire boundary layer, based on TBL estimation at the trailing edge of the suction side using Sagrado[16] experiments. A rotation of blocks 1 and 3, and although not represented in the Figure 1, is necessary for non-zero angle of attack to capture the wake which extends over 1.75 chords downstream. The obtained 2D mesh is almost uniform in the streamwise direction except in the vicinity of the TE. It is finally extruded in the spanwise direction using a constant cell size in the $z$-direction over a span length extend $L_z$. Note that the wall normal direction is stretched using a bi-geometric progression between each block. Periodicity condition is imposed in the $z$-direction and assessed not to influence the solution in section §IV.A.

We performed a mesh sensitivity analysis to evaluate the dependence of the measured quantities to the chosen grid resolution. We report in the Table 3, grid requirements as established by Wagner et al.[26] for DNS and LES (without additional wall-modeling) of an attached boundary layer, together with our choices of grids. Of course, these cell sizes requirement remain numerical scheme and thus code dependent, and need to be adjusted. Regarding LES, the quality of the results strongly depends on the value chosen for $\Delta x^+$ and $\Delta z^+$, since $\Delta y^+_{\min}$ should be equal to 1 in order to resolve the velocity gradients adequately at the wall to determine the level of turbulence production and hence the Reynolds stresses and wall friction reasonably. Indeed, a LES with $\Delta x^+ \leq 50$ and $\Delta z^+ \leq 12$ is considered by Wagner et al.[26] as an high-resolution LES yielding good agreement of predicted skin friction in plane channel compared to DNS or experiments. On the other hand, LES with $\Delta x^+ \geq 100$ and $\Delta z^+ \geq 30$ leads to unphysical streaks and large error in the skin friction according to Wagner et al.[26]

Since the turbulent structures evolving in the TBL are partially responsible for the wall-pressure fluctuations, it is necessary to capture the skin friction correctly and the resulting aerodynamic load. This directly translates to an accurate estimation of momentum thickness evolution.

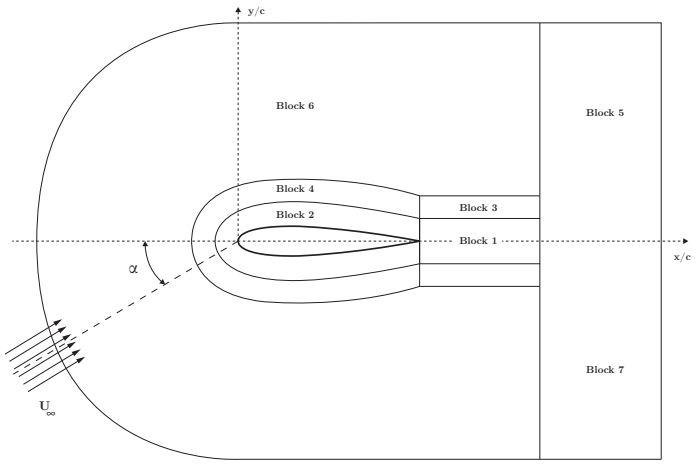


**Figure 1. Schematic 2-D diagram of the computational domain's blocking.**

To assess the grid resolutions, several meshes have been used and a comparison is proposed regarding the wall-normal $\Delta y^+_{\text{min}}$ and spanwise $\Delta z^+$ resolutions. The influence on the results of these grid spacings is investigated for the following resolutions $\Delta y^+_{min} = [1, 4, 10]$ and $\Delta z^+ = [10, 20, 30]$, in the wall-normal and spanwise direction, respectively. In order to validate the results, at $\alpha = 0°$, a comparison is made with experimental results of Sagrado[16] and with RANS computation performed on a 2D profile using Menter-SST turbulence model on a similar grid. We choose to perform the sensitivity analysis with a fixed streamwise resolution of $\Delta x^+ = 15$ in both cases, *i.e.* we consider only $\Delta y^+_{\text{min}}$ and $\Delta z^+$ variations, and a span length of $L_z = 0.02c$. Data from the LES computations are analyzed after an initial run of 2 convective time unit $t_c = c/U_\infty$, which ensures that the solution has reached a statistically steady state. Statistical quantities are then converged, averaging in both the spanwise homogeneous direction and time, during $3t_c$. In the present paper, for the sake of brevity, only the skin friction coefficient $C_f$ and TBL displacement and momentum thickness are plotted in Figures 2 and 3, respectively.

Figure 2 shows the $C_f$ distributions for $\Delta y^+_{\text{min}}$ and $\Delta z^+$ variations, compared with Sagrado[16]'s data which have been obtained using Clauser plots. In Figure 2(a), it can be observed a strong influence of the wall-normal resolution on the $C_f$ leading to an increasing underestimation with increasing $\Delta y^+_{\text{min}}$ grid spacing. However, in the Figure 2(b) the $C_f$ seems rather insensitive to the spanwise resolution $\Delta z^+$ and is in good agreement with Sagrado[16], except in the vicinity of the TE, and RANS data regardless of the grid spacing considered.

In order to better quantify the influence of $\Delta y^+_{\text{min}}$ and $\Delta z^+$ resolutions, the TBL displacement and momentum thickness are plotted in Figure 3. To extract the boundary layer displacement $\delta^*$ and momentum $\theta$ thickness, two methods are used to determine the boundary layer thickness $\delta$ as illustrated by Gloerfelt and Le Garrec[27]: a power-law fitting of the velocity profiles $\bar{u}/U_\infty = (y/\delta)^{1/n}$ inside the boundary layer ($y < \delta$) and a linear fitting on the free-stream velocity outside the boundary layer. The boundary layer thickness itself $\delta$ may be solely computed by the power-law, but using both fitting procedures increase the robustness in the boundary layer thickness which is further used to define $\delta^*$ and $\theta$, using the following definitions:

$$\delta^* = \int_0^\delta \left(1 - \frac{u(y)}{U_\infty}\right) \mathrm{d}y \quad \text{and} \quad \theta = \int_0^\delta \frac{u(y)}{U_\infty}\left(1 - \frac{u(y)}{U_\infty}\right) \mathrm{d}y$$

The same conclusion drawn from the $C_f$ can be observed for $\delta^*$ and $\theta$ in the Figure 3. The results are increasingly underestimating $\theta$ with the increasing $\Delta y^+_{\text{min}}$, as shown in Figure 3(a), whereas the TBL momentum thickness computed for the different spanwise resolutions is stable regardless the $\Delta z^+$ considered, see Figure 3(b). Regarding the TBL displacement thickness $\delta^*$, Figures 3(a) and 3(b), influence of the mesh resolution is non-monotonic on the estimation of $\delta^*$. However, it can clearly be seen that the spanwise resolution $\Delta z^+$ has only a weak effect on the flow dynamics whereas the wall-normal resolution $\Delta y^+_{\text{min}}$ has a direct effect on the $C_f$, $\delta^*$, and $\theta$, and must be carefully chosen. The mesh resolution chosen for the present work is set to: $\Delta x^+ = 15$, $\Delta y^+_{\text{min}} = 1$ and $\Delta z^+ = [10, 20]$ depending on the configuration and the span length considered.

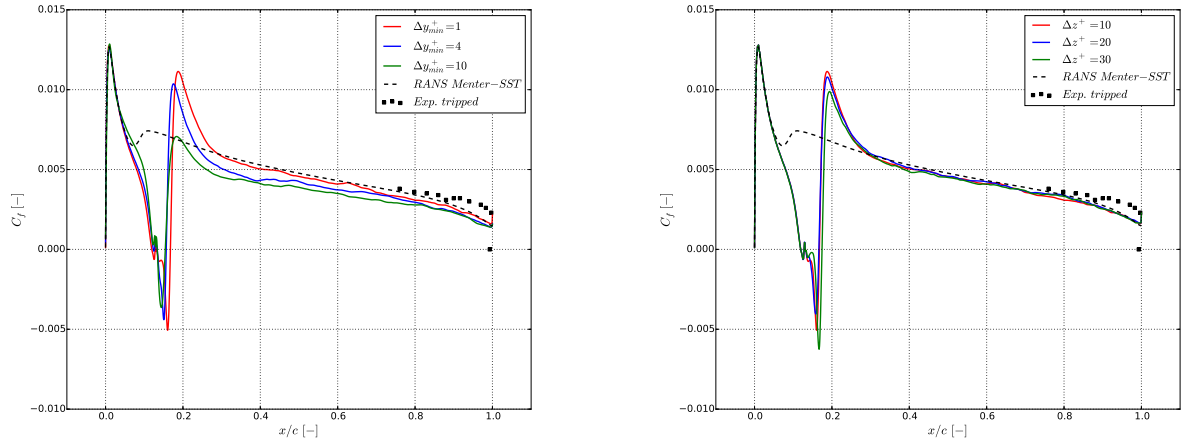


**Figure 2. Skin friction coefficient $C_f$ as a function of $x/c$ compared to Sagrado[16]'s experimental data for the tripped case and RANS calculation using Menter-SST turbulence model. (a) and (b) illustrate the influence of the wall-normal grid spacing for different $\Delta y^+_{min} = [1, 4, 10]$ (with fixed $\Delta x^+ = 15$ and $\Delta z^+ = 10$) and the spanwise grid spacing for different $\Delta z^+ = [10, 20, 30]$ (with fixed $\Delta x^+ = 15$ and $\Delta y^+_{\text{min}} = 1$), respectively.**

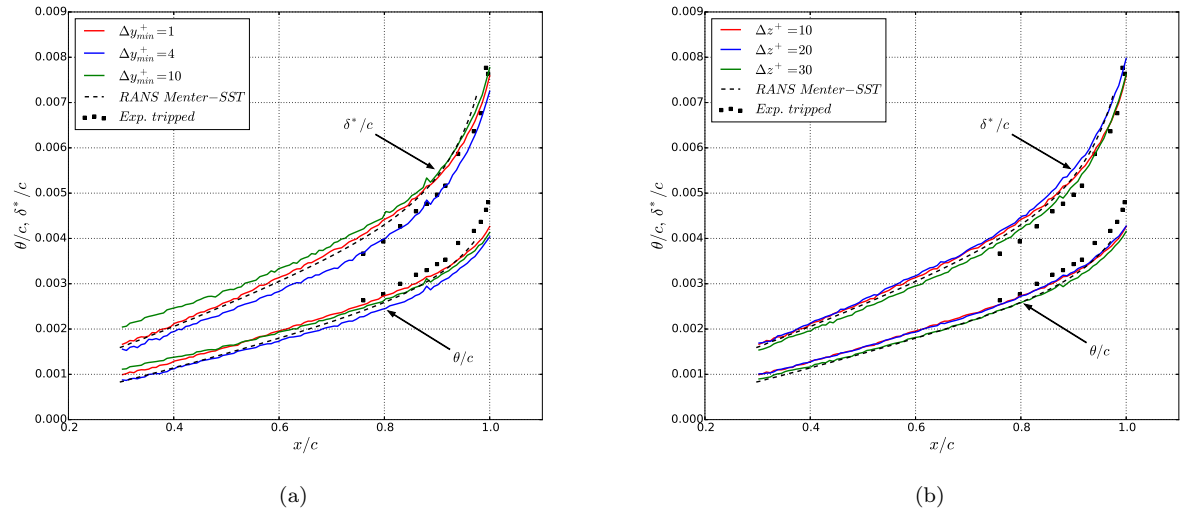


**Figure 3. Boundary layer displacement $\delta^*$ and momentum $\theta$ thickness compared to Sagrado[16]'s experimental data for the tripped case and RANS calculation using Menter-SST turbulence model. (a) and (b) illustrate the influence of the wall-normal grid spacing for different $\Delta y^+_{min} = [1, 4, 10]$ (with fixed $\Delta x^+ = 15$ and $\Delta z^+ = 10$) and the spanwise grid spacing for different $\Delta z^+ = [10, 20, 30]$ (with fixed $\Delta x^+ = 15$ and $\Delta y^+_{\text{min}} = 1$), respectively.**

## III.C. Data acquisition

In order to measure unsteady pressure signals from our computations, probes are placed in the first wall-normal cell along the airfoil. We acquire the pressure data along 101 spanwise lines of $N_z$ equidistant probes that are placed within the first cell on the upper surface of the airfoil. These pressure probes are referenced as **P0_x** where **x** is the index of the probe line, from $x/c = 0.6$ down to the TE ($x/c = 1.0$), see the Figure 4. The streamwise distribution of the probes, denoted by $\varepsilon_1$ is kept constant except in the vicinity of the trailing edge. Pressure probes are set to acquire pressure data every 50 timesteps $\Delta t$ such that the normalized sampling frequency is $f^*_s = t_c/(50\Delta t) \approx 6000$, *i.e.* we collect 6000 pressure samples per probe and convective time scale $t_c$.

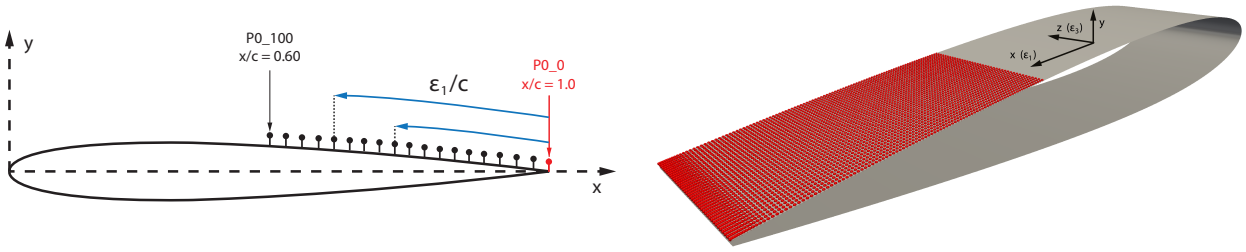


(a) (b)

**Figure 4. Probes are distributed in the streamwise direction from the TE ($x/c = 0.978$) up to $x/c = 0.60$ and in the spanwise direction covering the entire span. (a) Schematic streamwise pressure probes location for longitudinal analysis. (b) probes distribution on the upper side of the airfoil (span length not at scale).**

We first measure the cross-correlation coefficient $R_{p_ip_j}(\tau)$ defined by:

$$R_{p_ip_j}(\tau) = \frac{\langle p'_i(x_i,t)p'_j(x_j,t-\tau)\rangle}{p'_{i_{rms}}(x_i)p'_{j_{rms}}(x_j)} \tag{2}$$

with $\tau$ the time delay between the two considered signals $p'_i$ is the surface pressure fluctuation from probe $i$ located at position $x_i$, $p'_{i_{rms}}$ the root mean square of the pressure fluctuation measured by probe $i$ and $\langle\cdot\rangle$ denotes the time averaging. The cross-correlation is representative of the general dependence of the pressure fluctuation from one probe to the other. It provides information regarding characteristic scales of the wall-pressure related structures. Using $R_{p_ip_j}(\tau)$ it is possible to compute a convection velocity as a function of the separation distance $\varepsilon_1$ in the streamwise direction between probes. The convection velocity $U_c(\varepsilon_1)$ is then defined as:

$$\frac{U_c(\varepsilon_1)}{U_e} = \frac{\varepsilon_1/\delta^*}{[\tau U_e/\delta^*]_{\max}} \tag{3}$$

where $[\tau U_e/\delta^*]_{\max}$ denotes the time delay corresponding to the maximum of the cross-correlation $R_{p_ip_j}(\tau)$ between two signals separated by a distance $\varepsilon_1/\delta^*$.

Another important quantity is the wall-pressure coherence which is defined by:

$$\gamma^2_{ij}(f) = \frac{|\Phi_{p_ip_j}(f)|^2}{\Phi_{p_ip_i}(f)\Phi_{p_jp_j}(f)} \tag{4}$$

$\Phi_{p_ip_j}$ being the cross-spectrum between signals (obtained from the Fourier transform of the correlation function $R_{p_ip_j}(\tau)$) while $\Phi_{p_ip_i}$ is the autospectrum of each signal. $\gamma^2_{ij}(f)$ provides information about the frequency content of $R_{p_ip_j}(\tau)$, $0 \leq \gamma^2_{ij}(f) \leq 1$ and its square root is the normalized cross-spectrum between the two signals $p'_i(t)$ and $p'_j(t)$. In the present work, lateral coherence $\gamma^2(\varepsilon_3, St)$ will be mainly discussed since Brooks and Hodgson[5] and Wagner et al.[26] reported that the lateral coherence relates more specifically to the physical size of the eddies. This allows to compute a spanwise correlation length $l_z$ and provides further information about the TBL pressure patterns and associated flow structures. Note that the homogeneity in $z$ is leveraged to increase the convergence of the statistical sampling.

## IV. Flow characteristics

### IV.A. Minimum span length requirement

In order to perform reliable and accurate LES of a $z$-homogeneous configuration, it is important to assess that periodization does not affect the flow solution by using a wide enough domain span $L_z$. A characterization of the flow field is reported in this section for two different span lengths $L_z = 0.02c$ and $L_z = 0.06c$. This characterization is given, in the form of the resulting chord-wise evolution of the skin friction $C_f$, the shape factor $H_{12}$, the cross-correlation $R_{p_ip_j}(\tau)$, the spanwise coherence $\gamma^2(\varepsilon_3, St)$ and the spanwise correlation length $l_z$. Both simulations are performed using the parameters introduced in the previous section and

summarized in Table 2 with Vreman[25] SGS model and at $\alpha = 0°$. The spanwise resolution $\Delta z^+$has been doubled from $\Delta z^+ = 10$ to $\Delta z^+ = 20$ for the larger span length's case (though the span length is three-times wider) because of its previously commented weak influence and for obvious computational cost motivations. The total simulation time for both cases is $t = 4.3t_c$ after an initial run to converge towards a statistically steady state.

The skin friction coefficient and shape factor are plotted in Figure 5. One can observe that the span length as a moderate influence on the $C_f$, Figure 5(a), but the larger one allowed a better agreement with the experimental data from Sagrado[16] with a slight underestimation of the $C_f$ in the vicinity of the trailing edge. Another point of comparison is $H_{12}$, plotted in Figure 5(b), highlighting a rather important influence of the span length. Indeed, it can be observed, for $L_z = 0.06c$, that $H_{12}$ increasingly deviate from $L_z = 0.02c$ case as we move towards the TE. This is explain by the thickening of the boundary layer which reaches a height $\delta$, denoting the BL thickness, equal to the spanwise extend $L_z$ of the computational domain at approximately $x = 0.7c$. The overestimation of the shape factor is the results of slight underestimation of the BL momentum thickness $\theta$ whereas BL displacement thickness $\delta^*$ is perfectly fitting the experimental data for $L_z = 0.06c$, which are not shown in the present work for brevity.

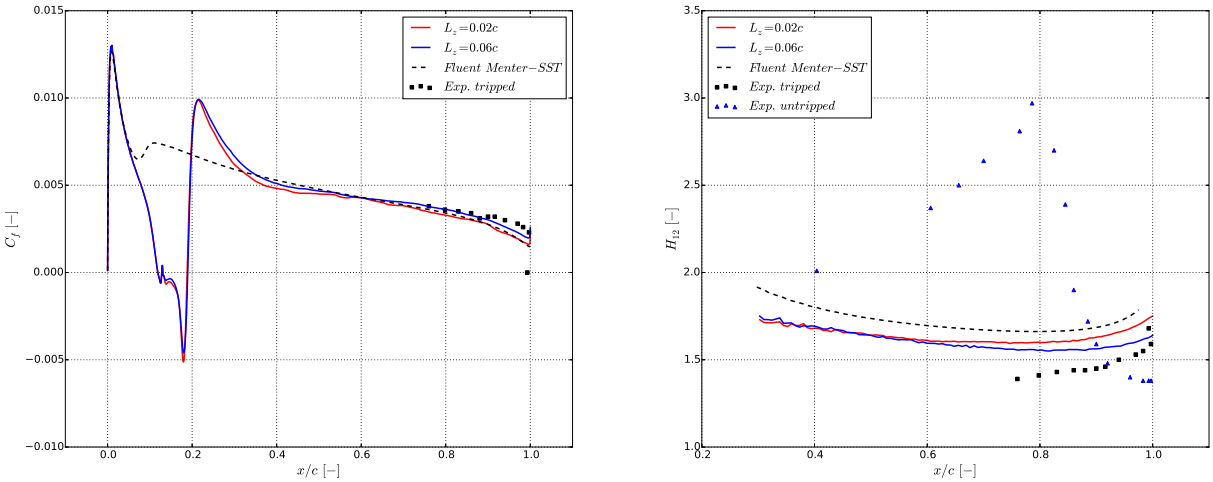


**Figure 5. (a) represent the skin friction coefficient $C_f$ as a function of $x/c$ for both span lengths considered and compared to Sagrado[16]'s experimental data for the tripped case and RANS calculation using Menter-SST turbulence model. (b) is the shape factor $H_{12} = \delta^*/\theta$ compared to Sagrado[16]'s experimental data for the tripped/untripped cases and RANS calculation using Menter-SST turbulence model.**

Another approach to characterize the influence of the span length is the analysis of the pressure signals recorded using the probes introduced in the computational domain. Pressure data, for both cases, are gathered over a total simulation time of $t = 4.3t_c$ convective time unit and divided in 8 overlapping segments with a 50% overlap. The cross-correlation coefficient $R_{p_i p_j}(\tau)$ is computed using probe P0_10 ($x = 0.978c$) as a reference for correlation with upstream probes separated by $\varepsilon_1$. The coherence function is computed for the spanwise distributed probes of P0_10 probe line, *i.e.* with the same streamwise location $x = 0.978c$.

One can clearly observe in Figures 6(a) and 6(c), the different decreasing rates of the maximum value of the cross-correlation coefficient with the separation distance $\varepsilon_1$. This rate relates to the change in the pressure signature, since the farther apart the probes, the larger the distance over which the structures can evolve and change, yielding to less correlated signals. For the narrower span, Figure 6(a), the pressure signals are correlated over a larger separation distance and thus for a greater time delay compared to the larger span. Since these $R_{p_i p_j}(\tau)$ plots take as a reference the probe line P0_10 at $x = 0.978c$, this observation can be explained by the fact that the lateral size of the domain $L_z$, which is approximately $0.5\delta$ in this region, constrains the size of the largest energetic structures. For $L_z = 0.06$, Figure 6(c), these structures can evolve more rapidly, without being constrained by the domain, leading to much lower correlation value of $R_{p_i p_j}(\tau)$ with increasing separation distance. Another interesting quantity is the spanwise coherence function $\gamma^2(\varepsilon_3, St)$ which gives an insight to the turbulent structures evolving in the BL since it relates to the physical size of the eddies as reported by Brooks and Hodgson[5]. In figures 6(b) and 6(d), are plotted the

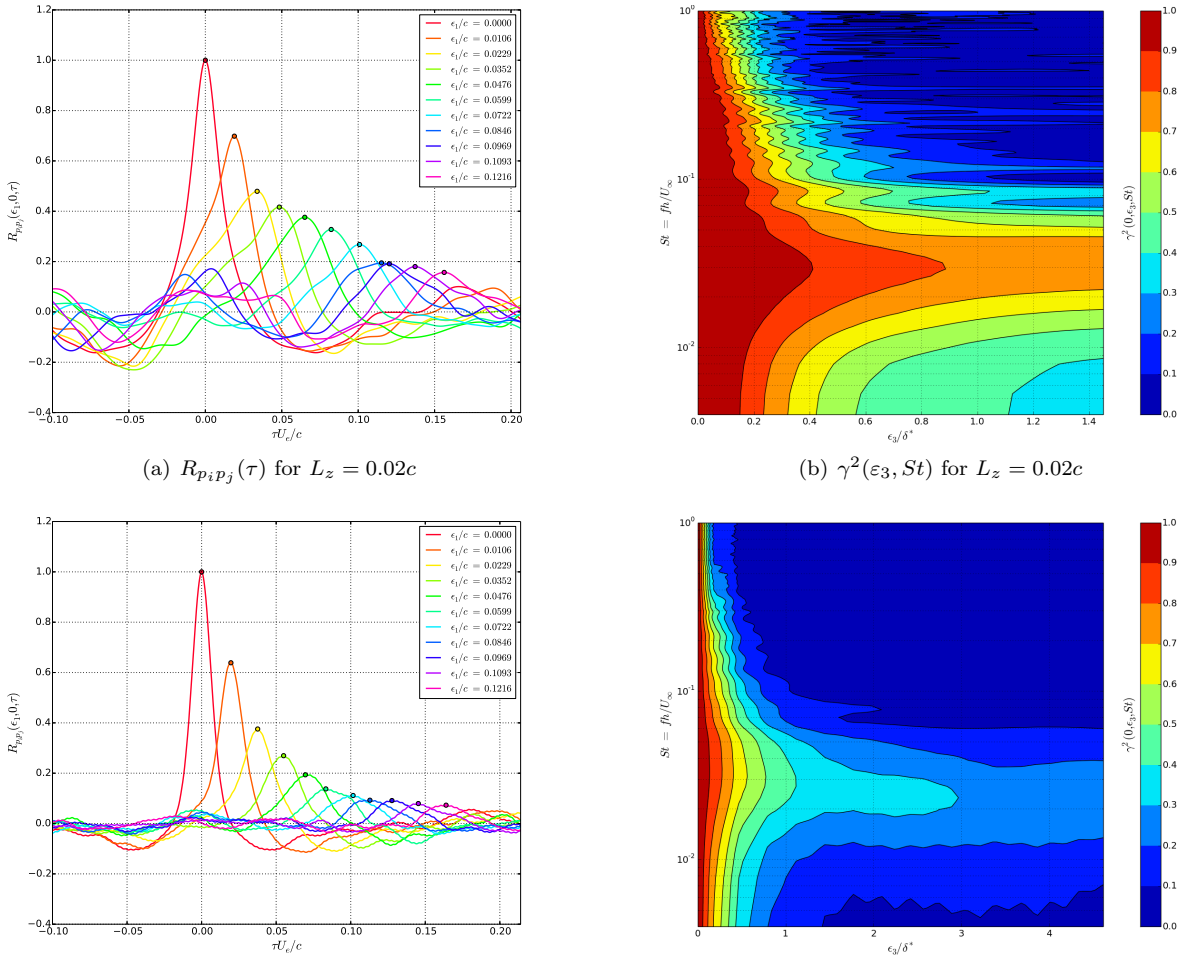


(a) $R_{p_ip_j}(\tau)$ for $L_z = 0.02c$

(b) $\gamma^2(\varepsilon_3, St)$ for $L_z = 0.02c$

(c) $R_{p_ip_j}(\tau)$ for $L_z = 0.06c$

(d) $\gamma^2(\varepsilon_3, St)$ for $L_z = 0.06c$

**Figure 6. (a) and (c) are the line plots of the cross-correlation coefficient $R_{p_ip_j}$ for different streamwise separation distance $\varepsilon_1$, the time delay $\tau$ has been normalised by the velocity $U_e$ at the edge of the boundary layer and the displacement thickness, $\delta^*$. (b) and (d) are the contour maps of the spanwise coherence function $\gamma^2(\varepsilon_3, St)$, the frequency is given by $St = fh/U_\infty$, with $h$ the TE thickness, and the lateral separation distance $\varepsilon_3$ is normalised by $\delta^*$. Probe P0_10 (closest to the TE, $x = 0.978c$) is the reference probe.**

contour maps of $\gamma^2(\varepsilon_3, St)$, as a function of frequency $St$ and lateral separation distance $\varepsilon_3$ for the reference probe line P0_10. One can observe for the highest frequencies ($0.1 < St < 1$) the coherence rapidly vanishes with increasing frequencies due to the decreasing scales of the eddies. For lower ones, a coherence ridge can be noticed around a particular frequency of $St \approx 0.03$ and $St \approx 0.025$, respectively in Figures 6(b) and 6(d), with a slower rate of decorrelation along the span compared to high and low frequencies. This ridge corresponds to the largest length scales evolving in the BL, with a characteristic frequency $f \sim \delta^{-1}$, as reported by Brooks and Hodgson[5]. For the lowest frequencies, no coherent structure can grow in the BL yielding to rapid decorrelation rate over the span.

Using the spanwise coherence function we can compute the spanwise correlation length $l_z$ by integrating $\gamma^2(\varepsilon_3, St)$ over the frequency range. This methodology have been sparsely used in the literature and should lead to more accurate results compared to the exponential fitting techniques commonly used. Two models have been selected for comparison and a brief description is given, more details can be found in the corresponding paper. Corcos[15] proposed a simple model for $l_z(\omega)$, Eq. (5), involving only the convection velocity $U_c$ of the turbulent structures responsible for the surface pressure field. In this model, $\alpha$ (or $b$) is a nondimensional parameter adjustable. This model have been extensively used in the literature but is only valid for high frequencies. Salze et al.[28] developed a model based on Efimtsov[29] to correctly evaluate $l_z$ over the whole frequency range, particularly in low frequency range, using pressure measurements on a flat plate with different pressure gradients. This model is giving the best results for the correlation length at low and

high frequencies. The model is given by Eq. (6) where $H_1 = \frac{\delta}{\delta^*}$ and the empirical constants $a_4$, $a_5$ and $a_6$ have to be defined using numerical/experimental data. The Salze model for the correlation length recovers Corcos[15] model at high $St_{\delta^*} = \omega\delta^*/U_\infty$ while admitting the physical lower bound $\delta^*/a_6$ for low $St_{\delta^*}$. The Corcos[15] model parameters used are $\alpha = 0.833$ and $U_c/U_\infty = 0.75$. For Salze et al.[28] model, the parameters used are identical as those defined in the paper; $a_4 = 0.85$, $a_5 = 100$ and $a_6 = 1$ and $U_c/U_\infty = 0.75$.

$$l_z = \frac{U_c}{\omega\alpha} = b\frac{U_c}{\omega} \tag{5}$$

$$\frac{l_z}{\delta^*} = \left[\left(\frac{a_4 St_{\delta^*}}{U_c/U_\infty}\right)^2 + \frac{a_5^2}{St_{\delta^*}^2\left(H_1^2 U_\infty/u_\tau\right)^2 + (a_5/a_6)^2}\right]^{-\frac{1}{2}} \tag{6}$$

Figure 7 shows $l_z$ computed from the present simulations, at $x = 0.978c$. For $L_z = 0.02c$, one can observe that $l_z$ is limited by the half spanwise extend of the domain $L_z/2$ for the largest integral scales aforementioned. Furthermore, discrepancies appear, for both span lengths, at high frequencies ($St_{\delta^*} > 1$) for which $l_z$ tends to an asymptotic value. Between cases $L_z = 0.02c$ and $L_z = 0.06c$ this asymptotic value is almost doubled, highlighting the direct dependency to the spanwise resolution which was doubled from $\Delta z^+ = 10$ to $\Delta z^+ = 20$. This asymptotic value corresponds to the size of three consecutive cells $3\Delta z^+$. The limits of Corcos[15] model can clearly be seen at the lowest frequencies whereas Salze et al.[28] model gives a perfect estimation of $l_z$ up to $St_{\delta^*} = 1$ for $L_z = 0.06c$.

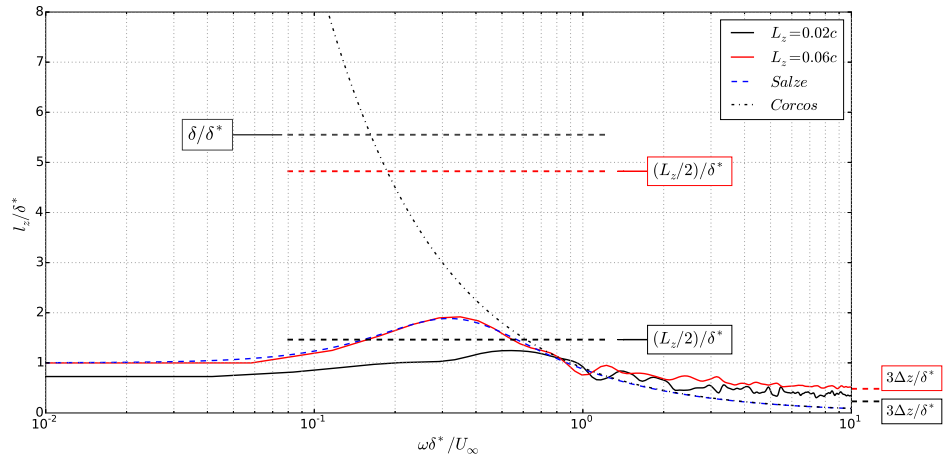


**Figure 7. Correlation length $l_z$ for span length $L_z = 0.02c$ and $L_z = 0.06c$ at $x = 0.978c$ compared to Salze et al.[28] and Corcos[15] models. $l_z$ is normalised using the spanwise averaged displacement thickness $\delta^*$ at P0_10 location and the frequency is given by $\omega\delta^*/U_\infty$. $\Delta z$ represents the size of one cell in the spanwise direction.**

Following the conclusions established in this section the span length influence is clearly visible especially for the lowest frequencies corresponding to the largest scales evolving in the boundary layer. According to the present results, the lateral length of the LES domain is set be at least $L_z/2 = 4\delta^*$ wide, corresponding to $L_z = 0.06c$ for $\alpha = 0°$, to enable sufficient signals decorrelation over the span as well as to prevent any spurious sustained levels of coherence.

### IV.B. Influence of the pressure gradient

In this part, we discuss an additional computation performed using $\alpha = 6.25°$ with an increased span length of $L_z = 0.1c$, consistent with the development of a thicker BL. Regarding outer layer scales, the domain has a similar span length $L_z/2 = 4.45\delta^*$, matching the above derived span length requirements. Apart from the angle of attack, simulations parameters and grid resolutions are kept identical for both cases, and the same post-processing procedures described in the previous section are used. In the Figure 8(a) and Figure 8(b), we report line plots of $R_{p_i p_j}(\tau)$. One can observe a slightly different rate of decorrelation for both angles with higher values of the peak of $R_{p_i p_j}(\tau)$ for larger $\varepsilon_1$ for $\alpha = 6.25°$. This illustrates that pressure fluctuation related structures remain correlated over larger separation distance and hence for longer time, consistent with the BL thickening. In the Figure 8(c) we extract the convection velocity $U_c$, see Eq. (3), as a function

of $\varepsilon_1$ normalised by $\delta^*$, taken at the reference probe line P0_10 ($x = 0.978c$), for both angles of attack. Using the $\delta^*$ length scale, $U_c(\varepsilon_1)$ presents a very similar behaviour except for very small distances $\varepsilon_1 < 5$. $U_c(\varepsilon_1)$ seems rather insensitive to pressure gradient variations, and reach an asymptotic value of approximately 0.75 ($\alpha = 0°$) and 0.72 ($\alpha = 6.25°$). One can observe a very good agreement with Sagrado[16]'s data for small $\varepsilon_1$. Discrepancies appearing for larger $\varepsilon_1$ are of comparable magnitude than the error induced by the relatively short time history (regarding large scale events) of the pressure signals used in this analysis. The lack of sampling is even more pronounced for $\alpha = 6.25°$, as $\delta^*$ is almost doubled in comparison with the symmetric case, making statistical convergence at large scales even more difficult to reach.

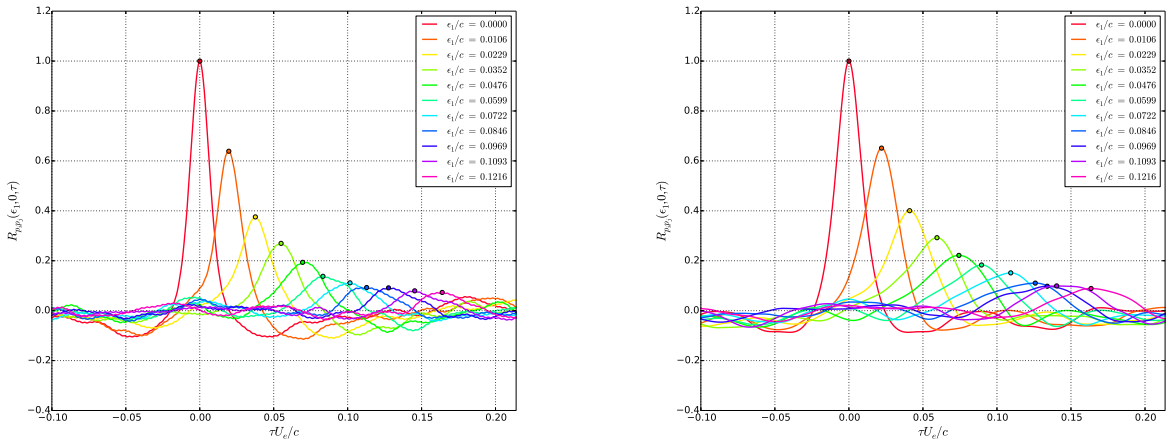


(a) $\alpha = 0°$ (b) $\alpha = 6.25°$

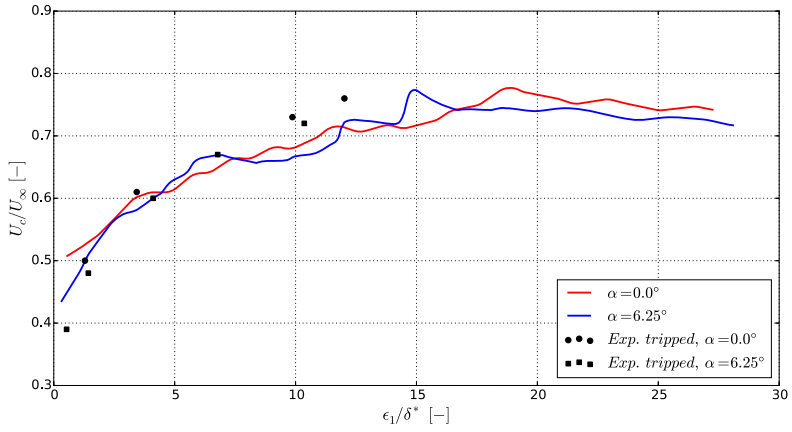


(c)

**Figure 8. (a) and (b) are the line plots of the cross-correlation coefficient $R_{p_i p_j}$ for different streamwise separation distance $\varepsilon_1$. (c) Convection velocity as a function of the longitudinal separation distance $\varepsilon_1$, normalised by $\delta^*$, for both angle of attack investigated $\alpha = 0°$ and $\alpha = 6.25°$ compared to Sagrado[16] experiments. Reference probe used for longitudinal spacing $\varepsilon_1$ and $\delta^*$ is P0_10 at $x = 0.978c$.**

Contour maps of the spanwise coherence function $\gamma^2(\varepsilon_3, St)$ for $\alpha = 0°$ and $\alpha = 6.25°$, at the same location on the suction side $x = 0.978c$, are plotted in Figure 9(a) and Figure 9(b), respectively. As observed previously, $\gamma^2(\varepsilon_3, St)$ presents the same general pattern for both angles of attack. The higher the frequency (the smaller the scale), the more rapidly the coherence decreases. We observe a large coherence ridge for both cases, which differs between $\alpha = 0°$ and $\alpha = 6.25°$ with $St = 0.025$ and $St = 0.015$, respectively. The reduction of this characteristic frequency is associated with the thicker BL on the suction side for $\alpha = 6.25°$ and thus larger scale structures of the TBL. An additional frequency peak appears with the increased angle of attack, with a second, smaller ridge of coherence appearing around $St = 0.06$, Figure 9(b). This narrow ridge is also present on Figure 9(a) at a frequency of $St = 0.08$ and may be related to the vortex shedding occurring at the TE in both cases. In the Figure 10(a) are plotted the spanwise and streamwise coherence of the pressure fluctuations at location $x = 0.978c$ with the same separation distance in both directions, $\varepsilon_1$=$\varepsilon_3$= $0.003c$.

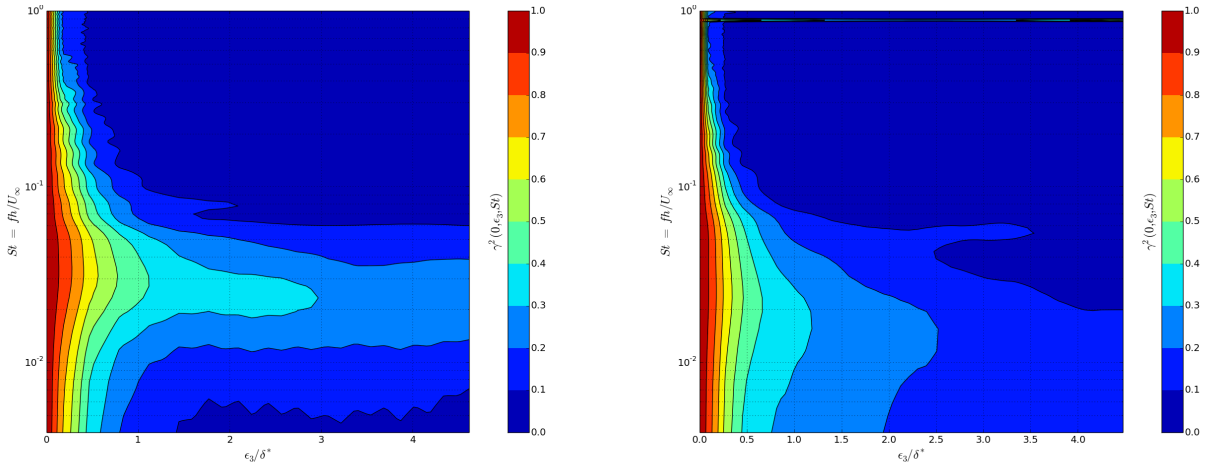


(a) $\alpha = 0°$ (b) $\alpha = 6.25°$

**Figure 9. Contour maps of the spanwise coherence function $\gamma^2(\varepsilon_3, St)$ on the suction side near the TE for probe line P0_10 ($x/c = 0.978$), for both angle of attack investigated: (a) $\alpha = 0°$ and (b) $\alpha = 6.25°$. The frequency is given by $St = fh/U_\infty$, with $h$ the TE thickness, and the lateral separation distance $\varepsilon_3$ is normalised by $\delta^*$.**

For a given probes spacing, the coherence is lower in the lateral direction. It highlights the fact that the coherence function relates to different aspects of the pressure field. The spanwise coherence $\gamma^2(\varepsilon_3, St)$ relates to the size (or scale) of the eddies whereas the streamwise coherence $\gamma^2(\varepsilon_1, St)$ relates more directly to the lifespan, or decay, of these eddies. Because eddies with the largest scales have the longest lifespan, these features of the surface pressure field are interrelated and the maximum of coherence occurs around the same frequency. Furthermore, the value of $\gamma^2(\varepsilon_1, St)$ is not unity, demonstrating that the convected TBL pressure field is not completely frozen. The eddies associated to lower frequency contributions appear to be changing character, or decaying, downstream but less rapidly than those with the highest frequencies. Finally, the increase of the pressure gradient is seen to affect the streamwise coherence for the higher frequency range by decreasing $\gamma^2(\varepsilon_1, St)$, indicating a shorter lifetime, *i.e.* higher decay rate, of the eddies which contributes to these frequencies. An opposite observation can be made for the spanwise coherence as the highest frequency range seems unaffected by the pressure gradient whereas the lowest range presents higher $\gamma^2(\varepsilon_3, St)$ values indicating larger structures in the TBL, which is thicker due to the adverse pressure gradient.

Figure 10(b) shows the coherence function between probes located at $x = 0.99c$ on the pressure and suction sides, P0_0 and L0_0. It can be seen that the coherence is rather small for the higher frequency range ($St \geq 0.2$) for both angles of attack and a peak appears $St = 0.1$ associated with the vortex shedding from the TE. This is in agreement with the value found by Brooks and Hodgson[5] and Sagrado[16]. The peak corresponding with the vortex shedding is obtained for smaller frequency for the non-zero AoA case. This is due to the chosen normalisation and associated variation of the bluntness parameter $h = 0.35\delta^*$ as opposed to $h = 0.6\delta^*(\alpha = 0°)$. The increased adverse pressure gradient and hence TBL thickness, only affects the low frequency range, highlighting larger scales evolving in the TBL.

As mentioned above, the lateral coherence function $\gamma^2(\varepsilon_3, St)$ is used to compute the spanwise correlation length $l_z$, which is plotted for both AoA cases in Figure 11, at $x = 0.978c$. We establish a comparison with the models of Salze et al.[28] and Corcos[15], with identical modelling parameters. With the strongest adverse pressure gradient, the highest frequencies exhibit the same asymptotic behaviour mentioned in section §IV.A, and related to the coherence between adjacent cells. However, in the mid-frequency range, the adverse pressure gradient seems to affect the frequency corresponding to the maximum $l_z$ by slightly shifting it to lower frequency, *i.e.* from $\omega\delta^*/U_\infty = 0.35$ to $\omega\delta^*/U_\infty = 0.30$. Regarding the lower frequency range the same asymptotic behaviour of $1\delta^*$ with decreasing frequency is found, as observed for $\alpha = 0°$.

Another interesting point of comparison is the power spectral density (PSD) plotted in Figure 12. The PSD is reported for the same different streamwise position, on the suction side, from the trailing edge at $x = 0.99c$ up to $x = 0.73c$ in Figure 12(a) and Figure 12(b) for $\alpha = 0°$ and $\alpha = 6.25°$, respectively. One can observe narrowband peaks in the higher frequency range, $St \geq 1$, which are the acoustic signature, fundamental and harmonics, of the vortex shedding occurring in the tripping area at $x = 0.127c$. Indeed, normalizing the frequency using the height of the source term previously introduced in place of the trailing

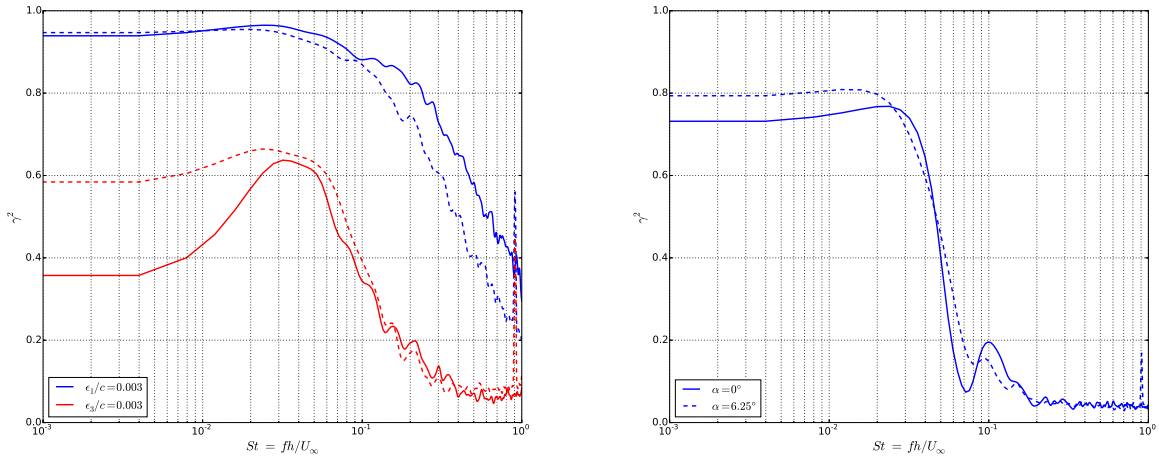


(a) (b)

**Figure 10. Coherence function $\gamma^2$, solid lines represents $\alpha = 0°$ results and dashed lines $\alpha = 6.25°$. (a) $\gamma^2$ for streamwise and spanwise aligned probes at $x = 0.978c$ with a separation distance of $\varepsilon_1$=$\varepsilon_3 0.003c$. (b) $\gamma^2$ between probes located at $x = 0.99c$ on the pressure (P0_0) and suction (L0_0) sides.**

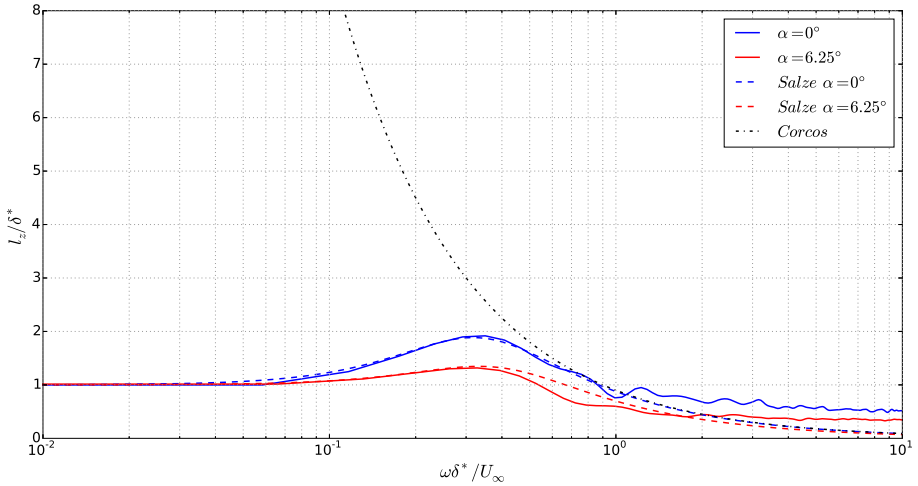


**Figure 11. Correlation length $l_z$ for the two angles of attack $\alpha = 0°$ and $\alpha = 6.25°$ at $x/c = 0.978$ compared to Salze et al.[28] and Corcos[15] models. $l_z$ is normalised using the spanwise averaged displacement thickness $\delta^*$ at P0_10 location and the frequency is given by $\omega\delta^*/U_\infty$.**

edge thickness, induces a first peak at $St' \approx 0.1$, characteristic of a bluff body vortex shedding. The signature of the airfoil induced shedding also appears for both AoAs with a maximum of the PSD (at location $x = 0.9983c$) at $St = 0.1$ exhibiting the vortex shedding occurring at the TE. One can observe an increase in the mid and low frequency energy content and a decrease at higher frequencies with increasing $x/c$ in both Figures 12(a) and 12(b). However, the shift on the PSD between the location closest to the TE and the point furthest upstream is larger for the non-zero AoA case, see Figure 12(b). This is due to the increase of the TBL thickness towards the TE and hence, the size increase of the biggest scales (*i.e.* lowest frequencies). This is translated into a shift of the energy content from the high frequencies to the lower ones, in agreement with Brooks and Hodgson[5] and Sagrado[16].

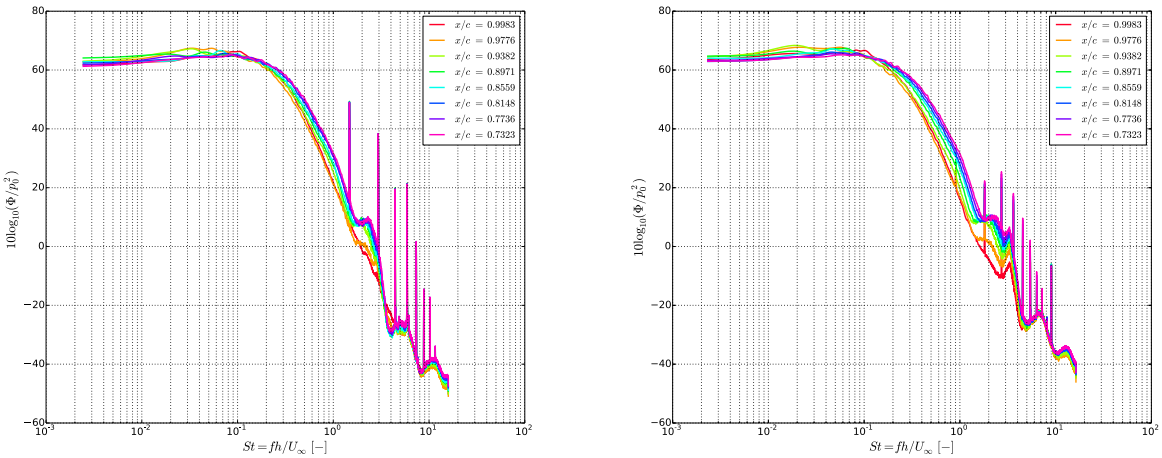


(a) $\alpha = 0.0°$ (b) $\alpha = 6.25°$

**Figure 12. Power spectral density referenced to $p_0 = 2 \times 10^{-5}$ $Pa$ at different streamwise positions for the two angles of attack $\alpha = 0°$ and $\alpha = 6.25°$.**

## V. Conclusion

We carried out large-eddy simulations to document the wall pressure fluctuations on a NACA0012 airfoil at $M = 0.05$ and flow conditions corresponding to a chord-based Reynolds number $Re_c = 4 \times 10^5$. We addressed the zero-load configuration for $\alpha = 0°$ and the $\alpha = 6.25°$ one to characterize the influence of the pressure gradient. The airfoil trailing edge is blunted with a bluntness parameter $h/\delta^* > 0.3$ which promotes vortex shedding. The laminar-turbulent transition was imposed at a fixed location $x_{tr} = 0.127$ by adding a sponge-like source term to the Navier-Stokes equations preserving both the geometry and the mesh topology. Spatial resolutions have been carefully chosen and the grid sizes set to $\Delta x^+ = 15$, $\Delta y^+_{\text{min}} = 1$ and $\Delta z^+ = [10, 20]$ to comply with literature facts about the streaks characteristic length scales in all directions. The span extent of the numerical domain has been verified to fulfill spanwise decorrelation of wall-pressure fluctuations only if $L_z/2 \geqslant 4\delta^*$. Thousands of numerical probes were distributed over the entire span between $x/c = 0.6$ and $x/c = 1.0$ and pressure signals were recorded over a period as long as $t = 4.3t_c$ with a normalized sampling frequency of 6000 samples per convective time-scale. The convection velocity $U_c$ displayed a significant increase with the separation distance $\varepsilon_1$ towards an asymptotic value at large distances that is robust to the influence of the pressure gradient, at least for the considered angle of attack. The spanwise correlation length $l_z$ computed from the present simulations were compared to Salze et al.[28] model which showed great capability to estimate $l_z$ over the entire frequency range and accounted very well for the effect of the pressure gradient. The observation by Sagrado[16] about the power spectral density are in line with the present study with, in particular, a characteristic decrease of the energy containing frequency towards the TE along the chord. The comprehensive database obtained from the present highly resolved large-eddy simulations have been validated against previous results and are giving credit to previously proposed sub-models for $U_c$, $l_z$ and $\Phi_{pp}$, themselves entering current noise prediction models. The extension of the present procedure to higher Mach numbers and more representative airfoil geometries is likely to help understanding how the features of near trailing edge boundary layer turbulence enters ingredients of the Amiet-type models and it should be helpful in developing new versions of TE noise models properly sensitized to the aerodynamic load or to compressibility effects.

## Acknowledgements

Authors would like to thank the continuous support and computational resources provided by CNRS on Turing (GENCI-IDRIS, Grant x20152a7178), Eos (CALMIP, Grant 2015-p1425).

# References


[1]Brooks, T. F., Pope, D. S., and Marcolini, M. A., "Airfoil self-noise and prediction," *National Aeronautics and Space Administration, Office of Management, Scientific and Technical Information Division*, Vol. 1218, 1989.

[2]Amiet, R. K., "Noise due to turbulent flow past a trailing edge," *Journal of Sound and Vibration*, Vol. 47, No. 3, 1976, pp. 387–393.

[3]Amiet, R. K., "Effect of the incident surface pressure field on noise due to turbulent flow past a trailing edge," *Journal of Sound and Vibration*, Vol. 57, No. 2, 1978, pp. 305–306.

[4]Howe, M. S., "A review of the theory of trailing edge noise," *Journal of Sound and Vibration*, Vol. 61, No. 3, 1978, pp. 437–465.

[5]Brooks, T. F. and Hodgson, T. H., "Trailing edge noise prediction from measured surface pressures," *Journal of Sound and Vibration*, Vol. 78, No. 1, 1981, pp. 69–117.

[6]Blandeau, V. P., *Aerodynamic Broadband Noise from Contra-Rotating Open Rotors*, Ph.D. thesis, 2011.

[7]Node-Langlois, T., Wlassow, F., Languille, V., Colin, Y., Caruelle, B., Gill, J., Chen, X., Zhang, X., and Parry, A. B., "Prediction of Contra-Rotating Open Rotor broadband noise in isolated and installed configurations," *20th AIAA/CEAS Aeroacoustics Conference*, , No. June, 2014.

[8]Kamruzzaman, M., Bekiropoulos, D., Lutz, T., Würz, W., and Krämer, E., "A semi-empirical surface pressure spectrum model for airfoil trailing-edge noise prediction," *International Journal of Aeroacoustics*, Vol. 14, No. 5-6, 2015, pp. 833–882.

[9]Roger, M. and Moreau, S., "Back-scattering correction and further extensions of Amiet's trailing-edge noise model. Part 1: theory," *Journal of Sound and Vibration*, Vol. 286, No. 3, sep 2005, pp. 477–506.

[10]Moreau, S. and Roger, M., "Back-scattering correction and further extensions of Amiet's trailing-edge noise model. Part II: Application," *Journal of Sound and Vibration*, Vol. 323, No. 1-2, 2009, pp. 397–425.

[11]Farabee, T. M. and Casarella, M. J., "Spectral features of wall pressure fluctuations beneath turbulent boundary layers," *Physics of Fluids A: Fluid Dynamics*, Vol. 3, No. 10, 1991, pp. 2410–2420.

[12]Leclercq, D. J. J. and Bohineust, X., "Investigation and Modelling of the Wall Pressure Field Beneath a Turbulent Boundary Layer At Low and Medium Frequencies," *Journal of Sound and Vibration*, Vol. 257, No. 3, Oct. 2002, pp. 477–501.

[13]Rozenberg, Y., Roger, M., and Moreau, S., "Rotating Blade Trailing-Edge Noise: Experimental Validation of Analytical Model," *AIAA Journal*, Vol. 48, No. 5, 2010, pp. 951–962.

[14]Aupoix, B., "Extension of Lysak's Approach to Evaluate the Wall Pressure Spectrum for Boundary Layer Flows," *Flow, Turbulence and Combustion*, Vol. 94, No. 1, 2014, pp. 63–78.

[15]Corcos, G. M., "The structure of the turbulent pressure field in boundary-layer flows," *Journal of Fluid Mechanics*, Vol. 18, No. 03, 1964, pp. 353–378.

[16]Sagrado, A. G., *Boundary layer and trailing edge noise sources*, Ph.D. thesis, Whittle Laboratory, 2007.

[17]Fischer, A., *Experimental characterization of airfoil boundary layers for improvement of aeroacoustic and aerodynamic modeling*, Ph.D. thesis, Technical University of Denmark, Department of Energy Engineering, 2011.

[18]Roger, M. and Moreau, S., "Broadband Self Noise from Loaded Fan Blades," *AIAA Journal*, Vol. 42, No. 3, 2004, pp. 536–544.

[19]Moreau, S. and Roger, M., "Effect of Airfoil Aerodynamic Loading on Trailing Edge Noise Sources," *AIAA Journal*, Vol. 43, No. 1, 2005, pp. 41–52.

[20]Rozenberg, Y., Roger, M., and Moreau, S., "Effect of blade design at equal loading on broadband noise," *Proceedings of the 12th AIAA/CEAS aeroacoustics conference, Cambridge, Massachusetts. AIAA Paper*, No. 2006-2563, 2006.

[21]Rozenberg, Y., *Modelisation analytique du bruit a erodynamique a large bande des machines tournantes : utilisation de calculs moyennes de mecanique des fluides*, Ph.D. thesis, 2007.

[22]Bermejo-Moreno, I., Bodart, J., and Larsson, J., "Scaling compressible flow solvers on the IBM Blue Gene/Q platform on up to 1.97 million cores," *Annual Research Briefs*, 2013, pp. 343–358.

[23]Larsson, J., Laurence, S., Bermejo-Moreno, I., Bodart, J., Karl, S., and Vicquelin, R., "Incipient thermal choking and stable shock-train formation in the heat-release region of a scramjet combustor. Part II: Large eddy simulations," *Combustion and Flame*, Vol. 162, No. 4, apr 2015, pp. 907–920.

[24]Larsson, J., Kawai, S., Bodart, J., and Bermejo-Moreno, I., "Large eddy simulation with modeled wall-stress: recent progress and future directions," *Mechanical Engineering Reviews*, , No. 0, 2015.

[25]Vreman, A. W., "An eddy-viscosity subgrid-scale model for turbulent shear flow: Algebraic theory and applications," *Physics of Fluids*, Vol. 16, 2004, pp. 3670–3681.

[26]Wagner, C., Huttl, T., and Sagaut, P., *Large-Eddy Simulation For Acoustics*, Vol. 20, Cambridge University Press, 2007.

[27]Gloerfelt, X. and Le Garrec, T., "Trailing Edge Noise from an Isolated Airfoil at a High Reynolds Number," *15th AIAA/CEAS Aeroacoustics Conference (30th AIAA Aeroacoustics Conference)*, Vol. 3201, No. May, 2009, pp. 11–13.

[28]Salze, E., Bailly, C., Marsden, O., Jondeau, E., and Juvé, D., "An experimental characterization of wall pressure wavevector-frequency spectra in the presence of pressure gradients," *20th AIAA/CEAS Aeroacoustics Conference, AIAA Paper*, Vol. 2909, 2014, p. 2014.

[29]Efimtsov, B. M., "Characteristics of the field of turbulent wall pressure fluctuations at large Reynolds numbers," *Soviet Physics Acoustics*, Vol. 28, No. 4, 1982, pp. 289–292.